Analysis of a Dual Tendon-Driven Robotic Dolphin Tail: Omnidirectional Motions and Thrust Characteristics

Bingxiong Wang , Chuanyu Sun , Daoliang Li , and Jincun Liu , *Member, IEEE*

Abstract—The exceptional swimming agility observed in dolphins is primarily attributed to the flexibility of their tails. Drawing inspiration from this biological phenomenon, this letter introduces a novel dual tendon-driven robotic dolphin tail featuring a passive joint designed to facilitate omnidirectional motion. To accurately capture the motion state of the robotic dolphin tail, a three-dimensional kinematic model is developed based on the constant curvature model. The parameters are identified by collecting data from an inertial measurement unit (IMU) positioned at the end of the caudal peduncle of the robotic tail. A Central Pattern Generator (CPG) controller, incorporating position-based control output, is employed to perform the omnidirectional motion. To investigate the thrust characteristics during fluke motions, advanced six-axis force sensors are utilized to measure propulsion forces and pitch moments under two distinct conditions: with or without the passive joint and a flexible or rigid fluke. Experimental results reveal crucial findings: (1) The presence of passive joints proves indispensable for thrust generation, attributing to the generation of the attack angle. (2) While a flexible fluke reduces pitch moments in comparison to a rigid one, it also decreases thrust. The research can pave the way for the development of dolphin-like omnidirectional motions.

Index Terms—Tendon-driven, robotic dolphin tail, omnidirectional motions, thrust characteristics.

I. INTRODUCTION

THROUGH millions of years of evolution, aquatic creatures such as fish, whales, jellyfish, and so on have acquired body structures perfectly suited to their environment and remarkable maneuvering capabilities. Aquatic creatures inspire the propulsor designs of biomimetic autonomous underwater vehicles (BAUV) [1]. Dolphins have a streamlined body shape that is optimized for minimizing fluid resistance. By employing their highly developed tail and synchronized flipper movements, dolphins are capable of executing extremely versatile actions, such as fast swimming, sharp turning, and leaping out. According to records, dolphins can reach speeds exceeding 11 m/s. The turning speed of dolphins is as high as 450 °/s, and the turning radius is as low as 0.11 to 0.17 of the body length (BL). Dolphins' propulsive efficiencies are 0.75 to 0.90 [2]. The extraordinary agility and mobility displayed by dolphins have garnered significant interest from scientists across the globe, prompting extensive research into unraveling the intricacies of their movement mechanics.

Most of the existing underwater biomimetic robots employ rigid structures comprising multiple serial joints, with each joint driven separately. Through the coordinated control of these individual actuators, these robots effectively replicate the undulatory or oscillatory movements characteristic of aquatic creatures, such as body-caudal fin (BCF) or median pectoral fin (MPF) locomotion. Wang et al. [3] developed a gliding robotic dolphin featuring two pitch joints, facilitating underwater three-dimensional motion through a combination of gliding mode and dolphin-like mode. However, the intricate design of the joint structure poses a challenge. And the steering capability is confined to flippers, consequently restricting maneuverability. Zhang et al. [4] designed a robotic dolphin with seven joints, capable of achieving four distinct steering modes by combining various swinging patterns of the head joint and flipper joints. However, it does not match the rapid turning capability of real dolphins, which rely solely on their tails for swift maneuvers. While redundant actuators effectively mimic the undulating waves of fish or dolphin bodies, the incorporation of such redundancy increases both structural design complexity and power consumption during swimming, thereby hindering improvements in swimming efficiency. In their efforts to create highly agile and efficient underwater biomimetic robots, researchers have made significant progress in actuator technology. Innovations such as shape memory alloy actuators [5], magnetic actuators [6], and pneumatic actuators [7] have emerged as promising alternatives. These smart actuators may be preferred, but they suffer from the complexity of the manufacturing processes, the absence of efficient system modeling theories, and the limited driving torques.

The authors are with the National Innovation Center for Digital Fishery, China Agricultural University, Beijing 100083, China, also with the Key Laboratory of Smart Farming Technologies for Aquatic Animals and Livestock, Ministry of Agriculture and Rural Affairs, China Agricultural University, Beijing 100083, China, also with the Beijing Engineering and Technology Research Centre for Internet of Things in Agriculture, Beijing 100083, China, and also with the College of Information and Electrical Engineering, China Agricultural University, Beijing 100083, China (e-mail: wangbingxiong@cau.edu.cn; chuanyu_sun@cau.edu.cn; dliangl@cau.edu.cn; liujincun@cau.edu.cn).

Inspired by the remarkable propulsive force generated by organisms in nature through the simple tensioning of tendons, researchers have designed a tendon-driven actuator. Comprising one or more sets of tendons, the tendon-driven actuator features a straightforward structure. Tendons are often made of lightweight materials, resulting in low inertia and excellent maneuverability. These advantages make the tendon-driven actuator highly suitable for BAUVs, garnering widespread attention from researchers. In 2017, Zhong et al. [8] proposed a biomimetic robotic fish that utilized a servo motor to drive parallel tendons for reciprocating motion. They established a two-dimensional kinematic model. In 2020, Shintake et al. [9] elaborated a simple biomimetic robotic fish. The intersection between the tendons and ribs of this biomimetic robotic fish was fixed, and the stiffness could be altered by changing the cross-sectional area of the tendons. In 2021, Wu et al. [10] delivered a high-speed soft robotic fish that utilized a brushless motor to continuously rotate and drive two gears in opposite directions, resulting in reciprocating tendon motion. The maximum cruising speed of this robotic fish was 2.02 BL/s. However, this design is limited to two-dimensional straight-line swimming and lacks the ability to perform yaw and pitch maneuvers. In 2022, Liao et al. [11] designed a wire-driven elastic robotic fish called "WE-Rofi". It simulated fish muscles using two sets of wires and incorporated a spine design based on elastic components. This design allows for both C-shaped and S-shaped undulations. In 2023, Yu et al. [12] fabricated a tendon-driven robotic fish with a controllable stiffness caudal fin. The motion of the robot fish was optimized using A-CPG and passive stiffness adjustment rules, resulting in improved turning radius and forward swimming speed. However, the swimming remains confined to the same plane. Nearly all existing biomimetic actuators for underwater robots employ a parallel tendon design situated in the same plane. This design choice restricts the tail's movement to two dimensions, providing limited assistance to researchers focused on exploring planar locomotion. In contrast, the dolphin tail's movements during propulsion and steering are not in the same plane. To meet this requirement, the robotic dolphin tail must exhibit omnidirectional motion capabilities, demanding the incorporation of at least two sets of tendons positioned in non-coplanar arrangements.

To explore techniques for enhancing maneuverability and swimming efficiency in a robotic dolphin tail, we developed a dual tendon-driven robotic tail. Inertial measurement sensors (IMUs) are strategically placed at the end of the caudal peduncle and the fluke to continuously monitor angles, velocities, and accelerations during motion. The efficacy of the proposed methods was verified through experiments that incorporated improved control strategies informed by the kinematic model. The contributions of this letter can be summarized into the following three aspects: 1) A dual tendon-driven robotic dolphin tail equipped with passive joints has been designed and implemented. With the benefits of dual tendon-driven mechanisms, the robotic dolphin tail can achieve omnidirectional motion, thus fulfilling the prerequisite of high maneuverability. 2) A complete three-dimensional kinematic model for the dual tendon-driven robotic dolphin tail has been formulated, establishing a solid

basis for model-based control strategies. 3) The passive joint improves the effective propulsive force by generating an attack angle that causes an shift in propulsion amplitude. While a flexible fluke reduces pitch moments in comparison to a rigid one, it also decreases thrust.

II. MECHATRONIC DESIGN OF THE DUAL TENDON-DRIVEN ROBOTIC DOLPHIN TAIL

A. Overview of the Robotic Prototype

A flexible tail is a necessary condition for dolphins to achieve multimodal swimming. In order to reproduce the flexible tail of dolphins, a robotic dolphin tail using a tendon-driven structure is designed. The mechanisms are illustrated in Fig. 1(a) and 1(b). Modeled after the streamlined tail of the bottlenose dolphin, the dolphin tail is mainly composed of three parts: 1) The front part of the tail containing the driving mechanism, as shown in Fig. 1(c); 2) the caudal peduncle that mimics the tendon, as shown in Fig. 1(d); 3) the fluke containing the passive mechanism, as shown in Fig. 1(e).

The front part of the tail containing the driving mechanism carries a brushless motor and a servo motor. The tendon-driven mechanisms can be classified as unidirectional or reciprocating according to whether the servo or motor that pulls the tendon reciprocates or not. The unidirectional motion drive mechanism reduces wear and tear associated with reciprocating motion, allowing for higher efficiency in driving servos or motors and potentially a higher tail flap frequency. But the mechanism that determines the range of the tendon motion by the traction disk fixes the amplitude of the tail flap. Designing additional amplitude change mechanisms is complex, and the range of adjustable amplitudes is limited. To achieve omnidirectional motion, two sets of tendon-driven mechanisms are required. It not only increases the difficulty of designing and laying out the mechanism but also makes it difficult to achieve the required amplitude. The reciprocating motion drive mechanism determines the range of the tendon motion along the perimeter of the traction disk. It realizes larger amplitudes with a concise structure. Therefore, the reciprocating motion drive mechanism is chosen for the tendon-driven mechanisms. Due to the limited space at the front part of the tail, the brushless motor and servo motor are positioned perpendicular to the tendons and utilize a steering bearing seat to alter the direction of traction. The fixed seat is 3D printed using polylactic acid (PLA). The steering bearing seat, motor bracket and traction disk are made of stainless steel. The periphery of the fixed seat in the front part of the tail is equipped with grooves that securely hold and constrain the tightly tied knots of the skin ropes. To accommodate communication wires, the excess space on the front part of the tail's mounting base is hollowed out.

The caudal peduncle, mimicking the structure of tendons, is comprised of a spinal column that traverses the entire tail, vertebrae that support the skin, and tendons that enable tail movement. The universal joints, specially designed according to the dolphin structure, are connected in series on the NiTi alloy wire to form the spine. The vertebrae are fixed by two adjacent sets of universal joints. The size of the vertebrae is
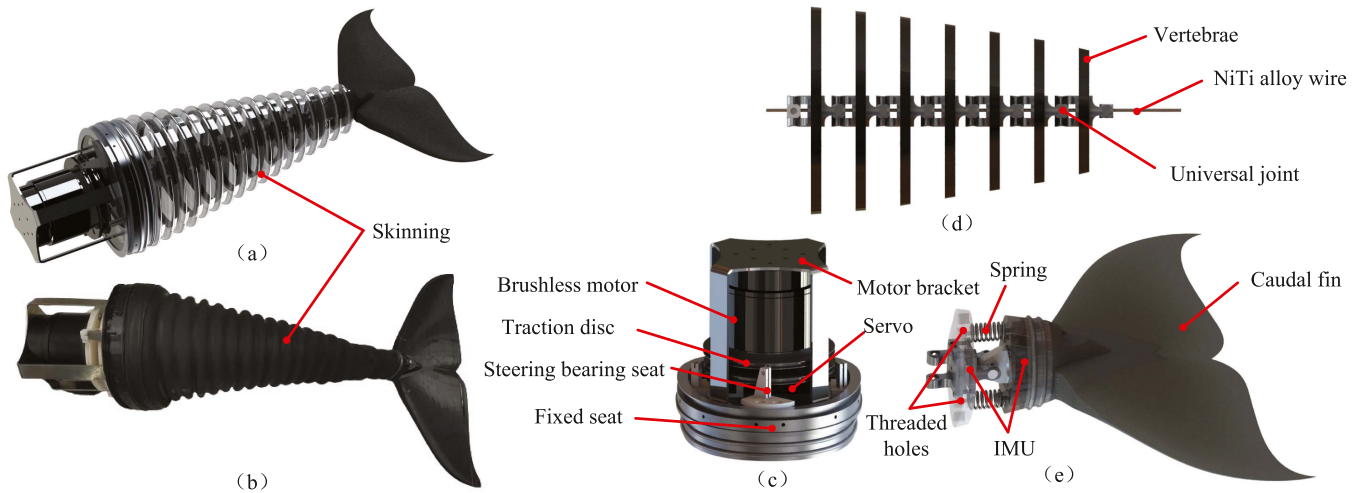
Fig. 1. Overview of the dual tendon-driven robotic dolphin tail. (a) Conceptual design. (b) Robotic prototype. (c) Front of the tail. (d) Caudal peduncle. (e) Fluke containing the passive joint.

TABLE I
TECHNICAL PARAMETERS OF THE DUAL TENDON-DRIVEN TAIL

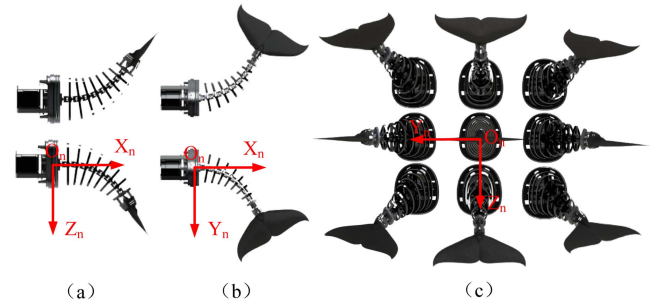| Items	Characteristics
Length× width× height	475 mm× 250 mm× 142 mm
Weight	1.42 kg
Number of vertebrae	7
Number of Passive joint	1
Spring constant	44.3 g/mm
Micro controller	STM32F407VGT6
Brushless motor	HT-S-6025
Servo motor	HS-7940TN
IMU	JY901
Communication module	E62(433 MHz)

Fig. 2. Design of the omnidirectional motion system. (a) Pitch motion. (b) Yaw motion. (c) Omnidirectional motion.

exactly determined according to the shape of the tail of the bottlenose dolphin. The tendon sequentially passes through seven vertebrae. The universal joints are made of stainless steel, the vertebrae are made of 3D printing, and the tendons are made of nylon threads.

The main controller of the system features an embedded processor utilizing the ARM architecture and operating on the FreeRTOS system. The motor communicates with the main controller through Controller Area Network (CAN). The IMU transmits data to the main controller through the serial port. The main controller controls the servo through Pulse Width Modulation (PWM). The detailed parameters can be found in Table I.

B. Design of the Omnidirectional Motion System

To realize omnidirectional movement in a three-dimensional space, resembling the natural motion of a dolphin's tail, we deploy two sets of tendon-driven actuators. The brushless motor controls the pitch tendons, enabling the robotic dolphin's tail to perform pitch movements under the traction of these tendons, as shown in Fig. 2(a). The servo motor provides control over the yaw tendons, leading to yaw movements in the robotic dolphin's tail, which are achieved through the traction provided

by these tendons, as shown in Fig. 2(b). The robotic dolphin's tail achieves omnidirectional motion through the combined traction of the pitch and yaw tendons, as shown in Fig. 2(c).

According to the kinematic formula derived by Zhong et al. [13], it is evident that a larger diameter of the traction disc results in a faster response speed of the tendons. Consequently, the diameter of the traction disc is set to the maximum value attainable within the size limitations of the tail, specifically 80 cm. The research conducted by Tim et al. [14] revealed that using a tapered or constricted shape can effectively mitigate stress concentration, resulting in a more even distribution of bending angles across the vertebrae. The tendons sequentially pass through each vertebra from front to back. The vertical diameter of the dolphin caudal peduncle is larger than the horizontal diameter, and the ratio between the vertical and horizontal diameters progressively increases closer to the distal end. Therefore, an elliptical profile is chosen as the fundamental shape, deviating from the traditional circular profile. The implementation of a slanted tendon arrangement effectively induces curvature near the base of the caudal peduncle. The ends of the tendons are fixed on the last vertebrae of the caudal peduncle, and the fluke containing a passive joint is connected to it.
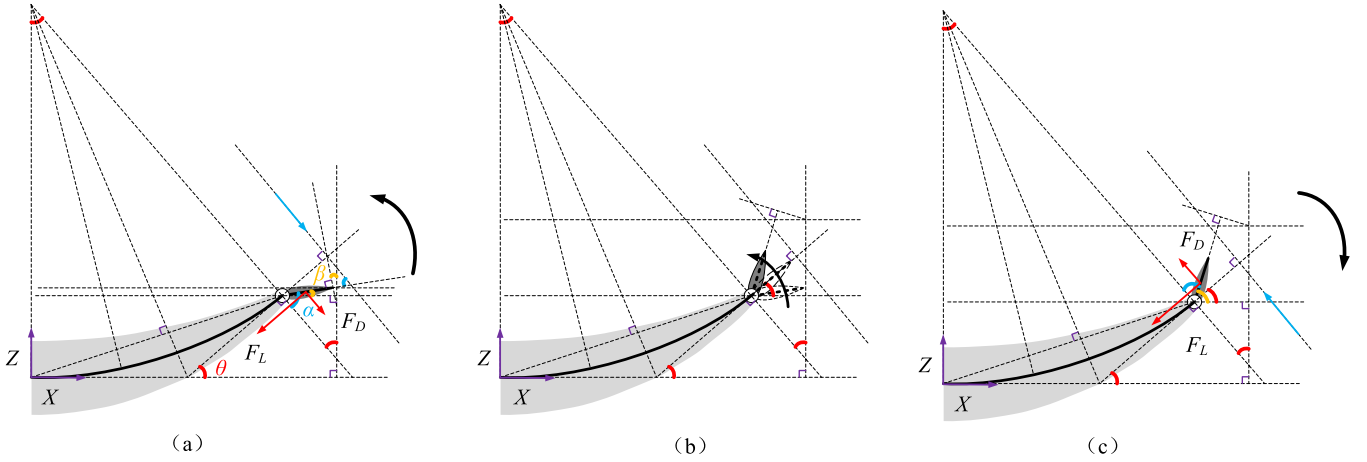
Fig. 3.   Half of a motion cycle. (a) Upward motion. (b) Endpoint. (c) Downward motion.

C. Design of the Passive Joint

The fluke containing the passive joint consists of a joint with springs and a fluke. Two springs with the same stiffness are installed symmetrically on both sides of the spine. In order to obtain real-time posture data of the tail during movement, two IMUs are mounted at both the end of the tail peduncle and the fluke. Threaded holes are strategically incorporated at fixed locations on the spring, allowing passive joints to be securely fastened by threading a long screw through the interior of the spring.

The passive joint at the connection point between the caudal peduncle and the fluke has been verified to significantly enhance swimming performance in underwater biomimetic robotic fish [15], [16]. In order to elucidate the mechanisms that underlie the improvement in swimming performance brought about by passive joints, our approach involves the quasi-steady approach, enabling us to discern the propulsive force and pitching moment generated during the locomotion process. Half of the pitch motion cycle of the robotic dolphin tail is illustrated in Fig. 3. During the upward motion as shown in Fig. 3(a), the caudal peduncle is pulled upward by the tendons, resulting in a deflection angle θ at the distal end of the caudal peduncle. The hydrodynamic forces exerted on the fluke cause the passive joint to rotate in the opposite direction. As a result, the deflection angle β of the fluke lags behind the angular deviation of the caudal peduncle. At the endpoint, as shown in Fig. 3(b), the caudal peduncle alters its motion direction under the influence of tendon traction. Simultaneously, the fluke, due to its inertia, maintains its original rotational direction, causing a disparity in angular deviation between the fluke and the caudal peduncle. During the downward motion as shown in Fig. 3(c), hydrodynamic forces acting on the fluke cause an angular difference to form between the fluke and the caudal peduncle. As the water flow direction is tangential to the distal end of the caudal peduncle, we can employ geometric principles to calculate the relationship between α, θ, and β:

$$\alpha = 90° - |\theta - \beta| \qquad (1)$$

According to the theory of lift-to-drag ratio, the attack angle α is recognized as a crucial parameter that characterizes lift
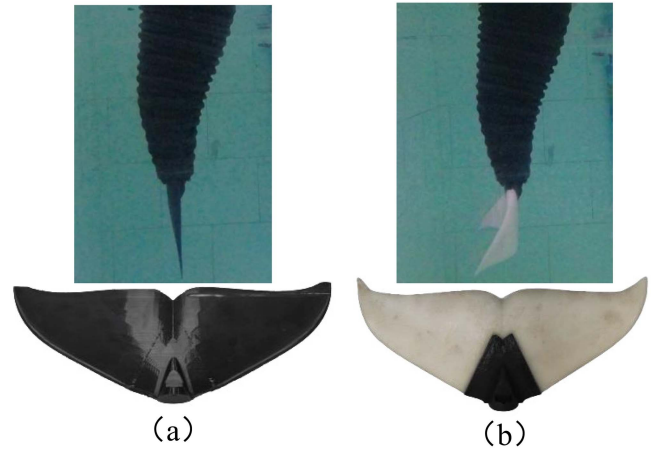

Fig. 4.   (a) Rigid fluke. (b) Flexible fluke.

and drag forces. Furthermore, thrust and pitch moments serve as expressions of lift and drag forces in a particular coordinate system. Therefore, by monitoring the changes in α during the motion, the mechanism of passive joints to increase propulsive force can be revealed.

The fluke is an important structure that affects propulsive forces and pitching moments. During movements, the fluke of a dolphin in nature deforms. We use a flexible fluke to mimic a real dolphin's fluke. The rigid fluke is 3D printed using PLA, which will not deform during movement, as shown in Fig. 4(a). Another kind of flexible fluke is made of silicone material with a Shore hardness of 40HA, which will deform during movement, as shown in Fig. 4(b).

III. KINEMATICS AND MOTION STRATEGIES

A. Kinematics of the Dual Tend-Driven Tail

The robot driven by the tendons is different from the traditional multi-joint robot composed of rigid joints and connecting rods, so it is not suitable for kinematics analysis with the DH method describing the rotation and translation joints [17]. The current mainstream modeling methods for tendon-driven
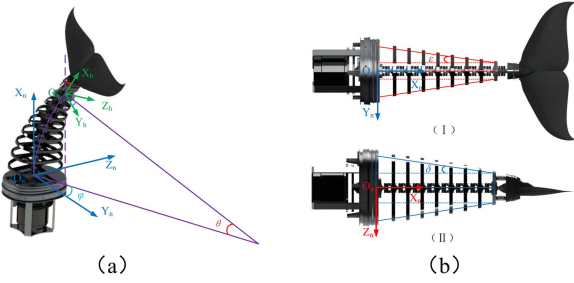
Fig. 5. Schematic illustration of the kinematic model. (a) Definition of the coordinate systems. (b) Tail top view I and side view II.

robots include the micro-element method, the constant curvature method, and the isogeometric method. The microelement and isogeometric methods have a large amount of calculation, which is not conducive to a fast solution. The expression of the constant curvature method is clear, which is conducive to engineering realization and experimental verification. Therefore, the tail of the robot dolphin is modeled using the constant curvature method, which is based on the following prerequisites:

(1) The distance between the vertebrae of the tendon-driven robot dolphin is equal. It is assumed that the vertebrae of the tail are connected by a continuous and smooth curve with equal curvature when the tail is bent.

(2) The NiTi alloy wire running through the spine of the tail has a constant curvature curve during the bending process.

The tail kinematics model is based on the caudal peduncle coordinate system and the fluke coordinate system, as shown in Fig. 5(a). When the tail is bent, the fluke coordinate system can be regarded as obtained by rotating the caudal peduncle coordinate system first around the x-axis by ϕ, then around the z-axis by θ, and finally around the x-axis by ϕ. l is the length of nickel-titanium alloy wire, and the homogeneous transformation matrix between the two coordinate systems is presented as follows:

$$R = R_{x,\phi}R_{z,\theta}R_{x,\phi} \tag{2}$$

$$d = \left(\frac{l}{\theta}s\theta, \frac{l}{\theta}c\phi(1-c\theta), \frac{l}{\theta}s\right)^\top \tag{3}$$

$$T = \begin{pmatrix} R & d \\ 0 & 1 \end{pmatrix}$$

$$= \begin{pmatrix} c\theta & -c\phi s\theta & -s\phi s\theta & \frac{l}{\theta}s\theta \\ c\phi s\theta & s^2\phi + c^2\phi c\theta & c\phi s\phi c\theta - s\phi c\phi & \frac{l}{\theta}c\phi(1-c\theta) \\ s\phi s\theta & s\phi c\phi c\theta - s\phi c\phi & s^2\phi c\theta + c^2\phi & \frac{l}{\theta}s\phi(1-c\theta) \\ 0 & 0 & 0 & 1 \end{pmatrix} \tag{4}$$

In order to make the equation more concise, this letter utilizes $c\phi$ as an abbreviation for $\cos\phi$, $s\phi$ for $\sin\phi$, $c\theta$ for $\cos\theta$, and $s\theta$ for $\sin\theta$. According to the kinematics model of the tail and the structure design of the traction disk that extends and contracts at the same time, the kinematic relationship from the driving space to the joint space and then to the operating space can be obtained. The inverse kinematic relationship can be derived by combining the kinematic relationships. A traction disc connects two opposite tendons at the same time. γ_1 and γ_2 are the angles

of the two traction discs, and r is the radius of the traction disc. When the traction disc rotates, one end retracts and the other end releases, so $\Delta l_1 = -\Delta l_3 = -r\gamma_1$, $\Delta l_2 = -\Delta l_4 = -r\gamma_2$. Δl_1, Δl_2, Δl_3, and Δl_4 are respectively the tendon 1, 2, 3, and 4 changes. When yaw motion and pitch motion are performed, respectively, the changes in the length of the tendons can be expressed by the following formulas:

$$c\varepsilon\Delta l_1 = l - l_1, l - l_1 = (\rho - \rho_1)\theta, \rho - \rho_1 = b$$
$$c\delta\Delta l_2 = l - l_2, l - l_2 = (\rho - \rho_2)\theta, \rho - \rho_2 = a \tag{5}$$

where a and b are the parameters to be identified, $\cos\varepsilon\Delta l_1$ and $\cos\beta\Delta l_2$ represent the projection of the extension and contraction of the tendon in the direction along the spine, ρ and ρ_i respectively represent the radius of curvature of the nickel-titanium alloy wire and the traction lines l when they are bent.

When the pitch and yaw motions are coupled in the robotic dolphin tail, the changes in the lengths of tendons can be expressed as follows:

$$c\varepsilon\Delta l_1 = b\theta c\phi$$
$$c\delta\Delta l_2 = a\theta s\phi \tag{6}$$

Combining the above formulas, the expression from the driving space to the joint space can be obtained as follow:

$$\begin{cases} \varphi = \arctan\left(\frac{b\gamma_2 c\delta}{a\gamma_1 c\varepsilon}\right) \\ \theta = \frac{r\gamma_1 c\varepsilon}{bc\varphi}(\theta = \frac{\gamma_2 rc\delta}{as\phi}) \end{cases} \tag{7}$$

B. Position-Based Motion Strategy

CPG is a distributed neural network that controls rhythmic behaviors in animals [18]. Its complexity lies between that of reflexes and higher-level central nervous systems. Vertebrate animals are capable of generating rhythmic movements without any feedback or active control. (7) gives the mapping of the driving space to the joint space. And (4) provides the mapping from the joint space to the operation space. Forward and inverse kinematics can be calculated by them. The CPG controller with position-based control output is used to control the output angle of the motor or servo. Therefore, the tail swing angles can be obtained from the motor and servo rotation angles according to the kinematic model. The dual tendon-driven robotic dolphin tail can be seen as controlled by two coupled neurons. The mathematical expression of a CPG model based on Hopf oscillators can be described as:

$$\begin{cases} \dot{x}_i = -\omega_i y_i + x_i\left(m_i - x_i^2 - y_i^2\right) + h_1\left(x_{i-1}c\varphi_i + y_{i-1}s\varphi_i\right) \\ \dot{y}_i = \omega_i x_i + y_i\left(m_i - x_i^2 - y_i^2\right) + h_2\left(x_{i+1}s\varphi_i + y_{i+1}c\varphi_i\right) \\ \zeta_i = k_i y_i \end{cases} \tag{8}$$

where x_i and y_i represent the oscillatory states of the i-th oscillator, ω_1 and m_i denote the oscillation frequency and intrinsic amplitude of the higher-level control commands, h_1 and h_2 are the coupling weights that determine the convergence speed, φ_i represents the phase lag between adjacent oscillators, k_i is the amplification coefficient, and ξ_i represents the tail swing angle i.e. θ and ϕ in three-dimensional space. The inappropriate values
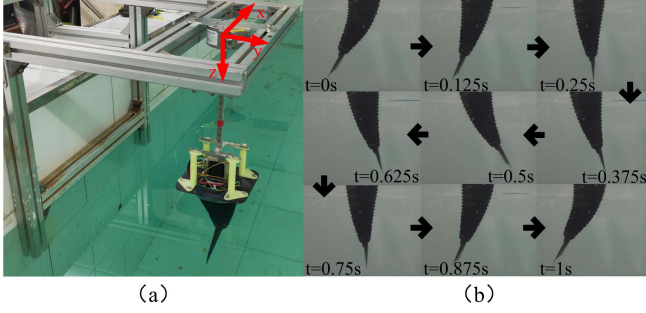
Fig. 6. Experimental setup. (a)Experimental platform. (b)Motion sequence of the rigid fluke with the passive joint over a cycle under the control parameters of $\theta = 30°$ and $f = 1$ Hz.

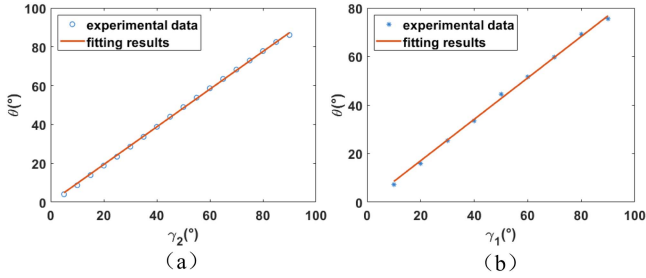Fig. 7. Process of parameter identification for the model. (a) Recognition of parameter b. (b) Recognition of parameter a.

of h_1, h_2, and k_i can cause the CPG controller to be unstable. So they are set to fixed values of 4, 5, and 6 respectively. Other parameters are set according to the needs of the movement.

IV. EXPERIMENTS AND ANALYSIS

The kinematic model proposed in Section III is effectively implemented in the tendon-driven robotic dolphin. Through underwater motion experiments with the robotic dolphin tail, the research examines the impact of passive joints and fluke stiffness on propulsion performance. By observing changes in the attack angle α, thrust, and pitching moment during the motion of the robotic dolphin tail, the research explores the principles for improving swimming performance via passive joints.

The experimental setup, as shown in Fig. 6(a), is a six-axis force sensor fixed above the water tank using a frame made of aluminum. The front end of the dual tendon-driven robotic dolphin tail is connected to the six-axis force sensor through a specially crafted mounting bracket. Both the caudal peduncle and the fluke are fully submerged in the water.

A. Model Parameter Determination and Verification

In order to obtain a kinematic model for the dual tendon-driven robotic dolphin tail that accurately reflects the actual motion pattern, a series of experiments are conducted to identify the model parameters. We sequentially set γ_i to change from $0°$ to $90°$ at $5°$ intervals for motors and $10°$ intervals for servos. An IMU is fixed at the end of the caudal peduncle to obtain the actual θ value. As a result, we derived the actual correspondence between γ_i and θ for each point as shown in Fig. 7. The identification of the unknown parameters a and b of the kinematic model is

TABLE II
PARAMETERS OF KINEMATIC MODEL

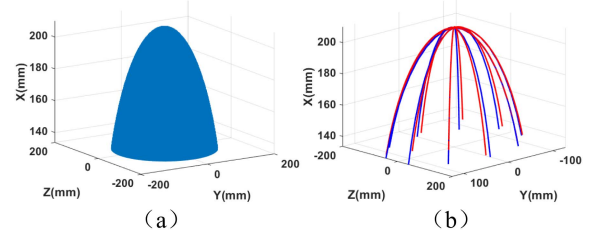| Parameter	l	r	ε	δ	a	b
value	210 mm	40 mm	0.1232	0.1512	40.9421 mm	46.3431 mm

Fig. 8. The verification of the kinematic model. (a) Range of the fluke motion. (b) Simulation trajectory and actual trajectory. The blue line indicates the simulation trajectory and the red line represents the actual trajectory.

performed using the least squares method. The mathematical expressions for parameter identification are derived from (7).

The identification of parameter b involves yaw motion. ϕ is a fixed value of $0°$. Parameter a relates to pitch motion. ϕ is a fixed value of $90°$. And the objective function can be described as:

$$J_1 = \text{minimize} \sum_{i=1}^{n} (\theta_i - f(\gamma_{1i}; b))^2$$

$$J_2 = \text{minimize} \sum_{i=1}^{n} (\theta_i - f(\gamma_{2i}; a))^2 \quad (9)$$

The results of parameter recognition are presented in Table II. The goodness of fit (R^2) and the root mean square error (RMSE) of the model of parameter b are 0.9982 and 0.9486, respectively. And the R^2 and the RMSE of the model for parameter a are 0.99949 and 0.57518, respectively.

With the coordinate system as the reference frame shown in Fig. 5, the motion space of the caudal peduncle's end is determined by the kinematic model, as depicted in Fig. 8(a). The motion space of the caudal peduncle's end is represented by an ellipsoidal surface, where the coordinates are constrained as follows: y ranges from -133.69 mm to 133.69 mm, z ranges from -133.69 mm to 133.69 mm, and x ranges from 133.69 mm to 210 mm. To confirm the efficacy of the kinematic model, we carry out simulations and actual experiments using a position-based motion strategy. The results are presented in Fig. 8(b). We conduct ten experiments according to equal intervals of ϕ and the same θ. The blue line indicates the simulation trajectory, and the red line represents the actual trajectory. The RMSE is 9.0963 mm.

B. Effect of Passive Joint and Fluke Material on Thrust Generation

To explore the influence of passive joint and fluke materials on the production of propulsive forces, a six-axis force sensor is utilized to quantify the forces and moments generated by water on a dual tendon-driven robotic dolphin tail while it is in motion. Four types of experiments are performed according to these two
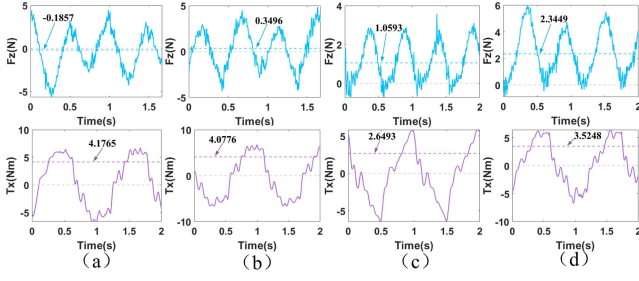
Fig. 9. Variations in F_z and T_x over two cycles under the control parameters of $\theta = 30°$ and $f = 1$ Hz. (a) Rigid fluke without passive joint. (b) Flexible fluke without passive joint. (c) Flexible fluke with passive joint. (d) Rigid fluke with passive joint. The mean values of F_z are marked with blue dashed lines and the means of the absolute values of T_x are marked with purple dashed lines.

Fig. 10. Statistical results for the mean value of F_z and the mean value of the absolute value of T_x. (a) The associated experimental data of F_z, frequency and angle. (b) The associated experimental data of T_x, frequency and angle.

different conditions. The associated motion sequence is shown in Fig. 6(b). The typical measurement results under the control parameters of $\theta = 30°$ and $f = 1$ Hz for a two-period motion are shown in Fig. 9. Since the z-direction of the six-axis force sensor is opposite to the direction of thrust, positive thrust is generated when F_z is less than 0. To enhance clarity, F_z takes its opposite number. Both propulsive force and pitching moment fluctuate periodically with the oscillation cycle of the fluke in all four Figs. In order to facilitate comparison, we chose the mean value of the average value and the absolute value of the pitch moment within two cycles as the evaluation indicators. All cases produce pitching moments between -6 Nm and 6 Nm. The amplitude of the pitching moment is independent of the passive joint and fluke materials. Comparison of Fig. 9(a) and 9(b) shows that the propulsive forces generated by both the flexible and rigid flukes during passive joint locking fluctuate roughly between -4 N and 4 N. The mean thrust generated by a flexible fluke is positive, while the mean thrust generated by a rigid fluke is opposite. The rigid fluke can't produce effective propulsion without the passive joint. The flexible fluke slightly improves effective propulsion and reduces pitching moments. However, in the comparison of Fig. 9(c) and 9(d), the flexible fluke reduces the pitching moment while reducing the propulsive force. It is related to the deformation of the flexible fluke during its movement. The comparison of Fig. 9(a) and 9(d) illustrates that the passive joint can significantly increase effective propulsive force over the flexible fluke. Throughout the entire motion cycle, the propulsive force is only negative for a brief period. And it is also evidenced by the comparative results of Fig. 9(b) and 9(c).

Because rigid fluke with the passive joint produces maximum propulsive force, It is chosen to conduct gradient experiments ranging from a frequency of 0.5 Hz to 3 Hz, with increments of 0.5 Hz, and amplitudes varying from $10°$ to $60°$, with increments of $10°$. The statistical analysis of the net values of each gradient during the motion of the rigid fluke with the passive joint is depicted in Fig. 10. It is evident from the graph that as the angle increases, both propulsive force and pitch moment become larger. Propulsive force tends to increase and then decrease with frequency. Because when the tail swings at a high frequency, the frequency of the passive joint responding to hydrodynamic forces to form a stable attack angle can't keep up with the frequency of the tail swing. When the frequency is 1.5 Hz and the angle is $60°$, the propulsive force reaches its maximum value,
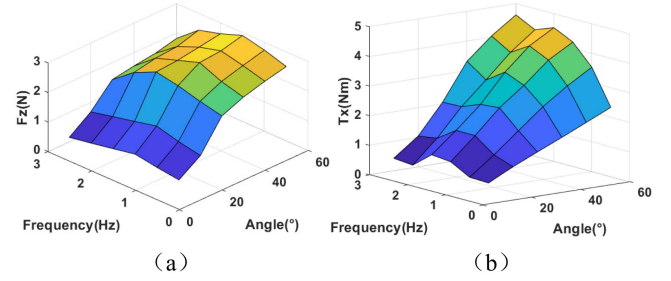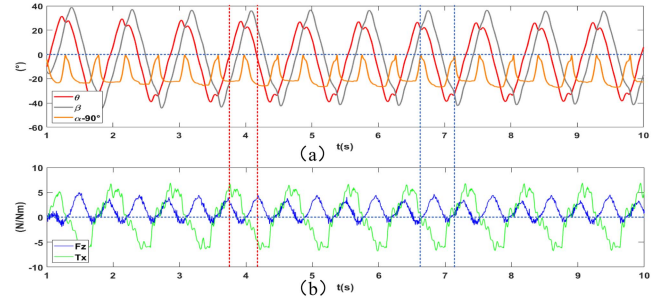

Fig. 11. Relationship between force/moment and motion parameters under the control parameter of $\theta = 30°$ and $f = 1$ Hz. (a) The movement trajectory of the robotic dolphin tail. (b) The variation of force/moment.

measuring 2.8996 N. The pitching moment shows a tendency to increase, then decrease, and then increase with frequency. When the frequency is 3 Hz and the angle is $60°$, the pitch moment reaches its maximum value, measuring 4.6113 Nm.

C. Analysis of Propulsive Force

In order to explore the mechanism by which passive joints enhance swimming performance, we integrate the force/moment data obtained from the six-dimensional force sensor with the data from two IMUs carried by the dolphin tail. The comparative analysis is presented in Fig. 11. For ease of presentation, the attack angles are presented as $\alpha - 90°$. The red vertical dashed line delineates a half cycle of motion starting in the center and ending in the center. From this half cycle, β consistently lags behind θ during the upward and downward motions. Hydrodynamic forces acting on the fluke drive the passive joint to rotate, constituting the phase lag. The phase lag produces α. When the tail swings to the center, the propulsive force and pitching moment are the largest. The blue vertical dashed line delineates a half motion from another phase. This half cycle begins at the endpoint of one side and ends at the endpoint of another side. It produces an α cycle corresponding to a propulsive force and pitching moment cycles. This means that α cycle is synchronized with the propulsive force and pitching moment cycles. When the attack angle is 0, the propulsive force and pitch moment are also 0. As the dolphin tail reaches the endpoint of one side and changes direction, the fluke continues its original rotation due to inertia. This stage corresponds to the stall phase, during which both propulsive force and pitch moment approach zero.

The experimental data are consistent with what we analyzed in Part II C.

D. Discussion

The robotic dolphin tail, in the absence of a passive joint, not only generated limited effective propulsive force but also caused overall uncoordinated motion. This issue arises because the fluke surface is always perpendicular to the direction of the water flow, resulting in the fluke experiencing only drag forces. The improvement in propulsive force is minimal even when a flexible fluke is paired with the passive joint locked. The passive joint significantly enhanced the effective propulsive force by inducing an attack angle, causing a shift in the amplitude of propulsion. The cycle of effective propulsive force generation is synchronized with the attack angle cycle. And the propulsive force is maximized when the tail swings to the center. However, at high swinging frequencies, the response frequency of the passive joint could not keep up with the tail's swinging frequency, leading to reduced propulsive force. Future research could consider transforming the passive joint into an actively controlled joint. Based on the existing kinematic model, attempts could be made to derive a dynamic model. Based on the dynamic model, a broader range of control strategies could be considered.

V. CONCLUSION AND FUTURE WORK

This letter details the design and creation of a dual tendon-driven robotic dolphin tail that can effectively achieve omnidirectional movements mirroring those of a real dolphin's tail. In order to enhance the understanding and performance of the dual tend-driven robotic dolphin tail, this letter establishes a complete three-dimensional kinematic based on the constant curvature model. The motion experiment of the dual tendon-driven robotic dolphin verified the effectiveness of the kinematic model. Then we explore the effects of the passive joint and fluke stiffness on the generation of propulsive forces. The cycle of effective propulsive force generation is synchronized with the attack angle cycle. The propulsive force is maximized when the tail swings to the center. While a flexible fluke reduces pitch moments in comparison to a rigid one, it also decreases thrust.

In the future, a complete dual tendon-driven robotic dolphin with an active control joint will be proposed. The dynamics of the entire dolphin will be considered. Moreover, future research will focus on investigating motion control approaches based on the model of the dual tendon-driven robotic dolphin.

REFERENCES

[1] M. Sfakiotakis, D. M. Lane, and J. B. C. Davies, "Review of fish swimming modes for aquatic locomotion," *IEEE J. Ocean. Eng.*, vol. 24, no. 2, pp. 237–252, Apr. 1999.

[2] F. E. Fish and J. Rohr, "Review of dolphin hydrodynamics and swimming performance," United State Navy Tech. Rep. 1801, 1999.

[3] J. Wang, Z. Wu, M. Tan, and J. Yu, "3-D path planning with multiple motions for a gliding robotic dolphin," *IEEE Trans. Syst., Man, Cybern. Syst.*, vol. 51, no. 5, pp. 2904–2915, May 2021.

[4] Z. Yang, W. Gong, H. Chen, S. Wang, and G. Zhang, "Research on the turning maneuverability of a bionic robotic dolphin," *IEEE Access*, vol. 10, pp. 7368–7383, 2022.

[5] S. Zhang, B. Liu, L. Wang, Q. Yan, K. H. Low, and J. Yang, "Design and implementation of a lightweight bioinspired pectoral fin driven by SMA," *IEEE/ASME Trans. Mechatron.*, vol. 19, no. 6, pp. 1773–1785, Dec. 2014.

[6] D. Romano, A. Wahi, M. Miraglia, and C. Stefanini, "Development of a novel underactuated robotic fish with magnetic transmission system," *Machines*, vol. 10, no. 9, 2022, Art. no. 755.

[7] A. D. Marchese, C. D. Onal, and D. Rus, "Autonomous soft robotic fish capable of escape maneuvers using fluidic elastomer actuators," *Soft Robot.*, vol. 1, no. 1, pp. 75–87, 2014.

[8] Y. Zhong, Z. Li, and R. Du, "A novel robot fish with wire-driven active body and compliant tail," *IEEE/ASME Trans. Mechatron.*, vol. 22, no. 4, pp. 1633–1643, Aug. 2017.

[9] J. Shintake, D. Zappetti, T. Peter, Y. Ikemoto, and D. Floreano, "Bio-inspired tensegrity fish robot," in *Proc. IEEE Int. Conf. Robot. Automat.*, 2020, pp. 2887–2892.

[10] S. C. Van Den et al., "Biomimetic design of a soft robotic fish for high speed locomotion," *Biomimetic Biohybrid Syst.*, vol. 12413, pp. 366–377, 2021.

[11] X. Liao, C. Zhou, Q. Zou, J. Wang, and B. Lu, "Dynamic modeling and performance analysis for a wire-driven elastic robotic fish," *IEEE Robot. Automat. Lett.*, vol. 7, no. 4, pp. 11174–11181, Oct. 2022.

[12] C. Qiu, Z. Wu, J. Wang, M. Tan, and J. Yu, "Locomotion optimization of a tendon-driven robotic fish with variable passive tail fin," *IEEE Trans. Ind. Electron.*, vol. 70, no. 5, pp. 4983–4992, May 2023.

[13] F. Xie, Z. Li, Y. Ding, Y. Zhong, and R. Du, "An experimental study on the fish body flapping patterns by using a biomimetic robot fish," *IEEE Robot. Automat. Lett.*, vol. 5, no. 1, pp. 64–71, Jan. 2020.

[14] Y. Sun, Y. Liu, and T. C. Lueth, "Optimization of stress distribution in tendon-driven continuum robots using fish-tail-inspired method," *IEEE Robot. Automat. Lett.*, vol. 7, no. 2, pp. 3380–3387, Apr. 2022.

[15] D. Chen, Z. Wu, Y. Meng, M. Tan, and J. Yu, "Development of a high-speed swimming robot with the capability of fish-like leaping," *IEEE/ASME Trans. Mechatron.*, vol. 27, no. 5, pp. 3579–3589, Oct. 2022.

[16] R. Tong et al., "Design and optimization of an untethered high-performance robotic tuna," *IEEE/ASME Trans. Mechatron.*, vol. 27, no. 5, pp. 4132–4142, Oct. 2022.

[17] S. Xu, B. He, Y. Zhou, Z. Wang, and C. Zhang, "A hybrid position/force control method for a continuum robot with robotic and environmental compliance," *IEEE Access*, vol. 7, pp. 100467–100479, 2019.

[18] J. Yu, M. Tan, J. Chen, and J. Zhang, "A survey on CPG-inspired control models and system implementation," *IEEE Trans. Neural Netw. Learn. Syst.*, vol. 25, no. 3, pp. 441–456, Mar. 2014.